Dalton Transactions

ROYAL SOCIETY OF CHEMISTRY

PAPER

View Article Online
View Journal | View Issue

Cite this: *Dalton Trans.*, 2026, **55**, 2908

Luminescent N-heterocyclic carbene Cu(I) complexes with N^O chelating ligands exhibit microsecond lifetimes and photocatalytic activity

Soumi Chakraborty,[a] Erqian Mao,[b] Thomas G. Gray[b] and Thomas S. Teets*[a]

To replace precious noble metal-based photosensitizers in applications involving photoinduced charge separation, energy transfer, or photocatalysis, Cu(I) complexes are considered to be cost-effective, earth-abundant, and sustainable alternatives. An emerging and effective design principle in Cu(I) photosensitizers involves heteroleptic structures where the HOMO and LUMO are spatially separated over two different ligands. In the present work, we introduce a complementary class of heteroleptic, three-coordinate copper photosensitizers that pairs variable N^O chelating ligands (8-hydroxyquinoline and 10-hydroxybenzo[h]quinoline) with a bulky 2,6-diisopropylphenyl-substituted N-heterocyclic carbene (NHC). In this design, both frontier orbitals are localized on the same ligand, the N^O chelate, such that structural modulation of the electron-rich N^O-chelates can substantially tune the energy levels of the HOMO and LUMO, thereby controlling the photoluminescence properties. Detailed photophysical and electrochemical experiments as well as DFT calculations suggest charge-transfer transitions with intraligand charge transfer (ILCT) character, involving the N^O ligands. This strategy successfully produced long triplet excited-state lifetimes (up to 44 μs) in compounds that are strong photoreductants ($E([Cu]^+/*[Cu]$ as negative as −2.0 V *vs.* the ferrocenium/ferrocene couple). These properties allow these photosensitizers to be used as photocatalysts in various transformations of organic compounds, such as hydrogenation of substituted benzophenones, hydrodehalogenation of aryl/alkyl halides (including challenging C–Cl bond activation) and *E*/*Z* isomerization of (*E*)-stilbene (an example of triplet–triplet energy transfer).

Received 15th December 2025,
Accepted 26th January 2026

DOI: 10.1039/d5dt02991k

rsc.li/dalton

Introduction

Molecular photosensitizers have a wide range of applications in fields that include materials science, biomedicine, photovoltaics, and synthetic chemistry.[1–5] For a long time, the design of homogeneous photosensitizers and photocatalysts primarily relied on precious transition metals such as iridium(III),[6,7] ruthenium(II)[8,9] and platinum(II).[10,11] These precious transition metals have demonstrated high efficiency as photocatalysts due to features that include strong absorption over the visible region and long excited-state lifetimes.[5,12] However, due to the high cost and low abundance of the noble metals, it is important to develop more sustainable and cost-effective approaches to design photosensitizers for large-scale applications. As such, there have been many prominent studies to introduce earth-abundant first row transition metals as cheaper alternatives to precious metals in various fields of chemistry. For the effective design of a photosensitizer, the main challenge associated with the 3d transition metals is to overcome nonradiative deactivation of the triplet excited state caused by low-lying metal-centered (MC) d–d transitions, observed when there are partially filled 3d orbitals.[5] In this context, Cu(I) complexes have gained significant attention due to their closed shell $3d^{10}$ electronic configuration that removes the possibility of deleterious MC states and makes it more straightforward to access long-lived charge-transfer transitions. As a result, Cu(I)-based photosensitizers have been successfully studied for solar cells, OLEDs, and photocatalytic reactions.[13–16] The majority of Cu(I) photosensitizers so far are four-coordinate pseudo-tetrahedral homo- and heteroleptic complexes featuring diimine (N^N) and diphoshphine (P^P) ligands. Detailed investigation of the photophysical processes of four-coordinate Cu(I) complexes supports a pseudo-Jahn–Teller flattening distortion in the excited state leading to the formation of a five coordinate exciplex, promoting fast nonradiative decay that decreases the excited state lifetime.[5] A common strategy to alleviate this problem is to introduce bulkier ligands in order to block the geometrical distortion of the excited state as well as to increase the lifetime.[13] An emerging approach that has gained recent

[a]*Department of Chemistry, University of Houston, Houston, Texas 77204, USA. E-mail: tteets@uh.edu*
[b]*Department of Chemistry, Case Western Reserve University, Cleveland, Ohio 44106, USA*

traction in the design of copper(I) photosensitizers involves heteroleptic structures combining one electron-rich anionic ligand with a neutral π-acceptor ligand; the ligands can be monodentate or bidentate, resulting in coordination numbers between two and four. Recent examples include four-coordinate copper(I) complexes combining diphosphines with anionic 4*H*-imadizolate chelates, capable of photoinduced charge accumulation,[17,18] and carbene metal amide (cMa) complexes that span the entire coinage metal series and include many examples of two-coordinate copper complexes that are luminescent[19,20] and function as solar photosensitizers.[21]

The usual situation in the types of heteroleptic copper complexes described above is that the HOMO is substantially localized on the electron-rich anionic ligand, with the LUMO localized on the neutral π-acceptor. A complementary approach to three-coordinate copper(I) photosensitizers places the electron-rich and π-accepting functionalities on the same anionic chelating ligand. With the frontier orbitals localized on the same ligand, the low-energy excited state is best described as intraligand charge transfer (ILCT), distinct from the more typical metal-to-ligand charge transfer (MLCT, commonly observed in homoleptic copper(I) chromophores) and ligand-to-ligand charge transfer (LL′CT, commonly observed in heteroleptic copper(I) chromophores). With ILCT excited states, both frontier orbitals are centered on the same ligand and thus can be tuned by structural modulation of that single ligand. In addition, LL′CT excited states sometimes suffer from low oscillator strengths when the donor (HOMO) and acceptor (LUMO) orbitals are perpendicularly oriented,[22] which is avoided in ILCT excited states involving planar ligands.

The work presented here introduces heteroleptic copper(I) complexes with ILCT excited states that exhibit long excited-state lifetimes and function as versatile photoredox catalysts. They are supported by hydroxy-substituted quinoline derivatives, 8-hydroxyquinoline and 10-hydroxybenzo[h]quinoline, and both are capped with the same bulky N-heterocyclic carbene (NHC), {1,3-bis(2,6-diisopropylphenyl)-1,3-dihydro-2*H*-imidazol-2-ylidene} (IPr). This and related NHC ligands have been extensively used in other classes of copper(I) charge-transfer chromophores,[19,20,23–34] and we hypothesized that its strong σ-donor ability and large steric profile would be important for stabilizing three-coordinate structures and promoting long excited-state lifetimes. Two Cu(N^O)(IPr) complexes are presented in this work, cataloguing their electrochemical and photophysical properties, supplemented by DFT calculations, with applications in photocatalytic reactions of organic compounds. The copper(I) center facilitates intersystem crossing to a ^{3}ILCT state, allowing these compounds to exhibit long-lived phosphorescence (lifetimes up to 44 μs). These complexes are also predicted to be strong photoreductants ($E([Cu]^+/*[Cu])$ = −1.8 V to −2.0 V). The long excited-state lifetimes facilitate good photocatalytic reactivity for an energetically uphill alkene isomerization reaction that involves triplet–triplet energy transfer, and the strong excited-state reducing capability enables reductive photoredox transformations to be carried out on different substrate classes. The copper(I) complexes disclosed here represent a new structural-class of charge-transfer chromophores with attractive photophysical properties and good excited-state reactivity.

Results and discussion

Synthesis and structural characterization

The synthesis of the heteroleptic copper complexes is outlined in Scheme 1, with more details in the experimental section. First, the neutral N^O ligand precursors are treated with either benzylpotassium or NaHMDS (HMDS = bis(trimethylsilyl)amide) in a 1 : 1 ratio to obtain the respective potassium or sodium salt. These salts are combined with chloro[1,3-bis(2,6-diisopropylphenyl)imidazol-2-ylidene] copper(I), Cu(IPr)Cl, in a 1 : 1.2 ratio in anhydrous THF, stirring for 24 hours at room temperature. Following purification, the desired products were obtained in good yields, as specified in Scheme 1. Both complexes (**Cu1** and **Cu2**) are sensitive to aerobic conditions and are best stored inside a nitrogen-filled glovebox. The complexes were characterized by ^{1}H and ^{13}C{^{1}H} NMR spectroscopy (Fig. S47–S50), which are consistent with the proposed structures and confirm their purity. High-resolution mass spectrometry was attempted on **Cu1** and **Cu2**, but in both cases the only ion observed has an *m*/*z* value of *ca.* 492.24, which corresponds to the ligand-substitution product [Cu(IPr)(MeCN)]$^+$ (Fig. S61 and S62), indicating the compounds are not stable in MeCN.

The structural features of **Cu1** and **Cu2** were further characterized by single-crystal X-ray diffraction, and the molecular structures are illustrated in Fig. 1. Table S1 summarizes refinement parameters, and Table S2 collects the bond lengths and angles involving the copper center. The coordination environment in both complexes is planar, with the sum of the bond angles around the copper center very near 360°. The best

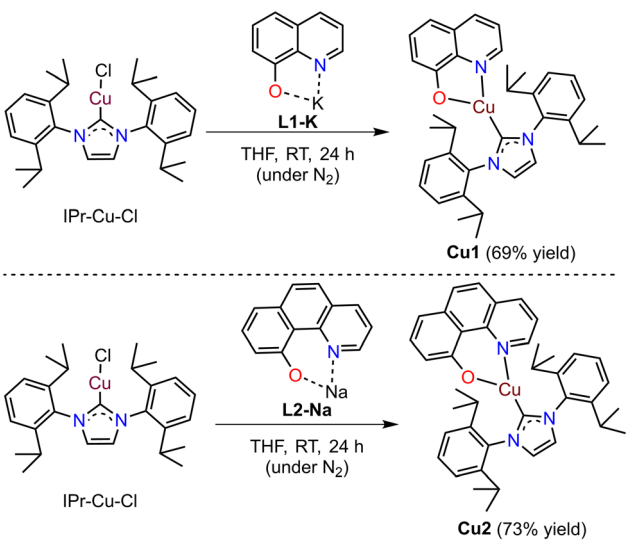

Scheme 1 Synthesis of Cu(I)–NHC complexes using N^O chelating ligands.

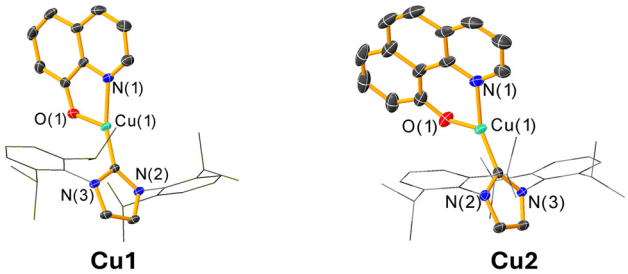

Fig. 1 Molecular structures of **Cu1** and **Cu2** determined by single crystal X-ray diffraction. Thermal ellipsoids are shown at the 50% probability level.

descriptor of the coordination geometry is distorted Y-shaped. The smallest bond angle about copper is imposed by the N^O chelate ring, giving an N–Cu–O angle of 82.87(7)° in **Cu1** (five-membered chelate) and 90.32(7)° in **Cu2** (six-membered chelate). There is a significant disparity between the other two bond angles about the copper vertex, in which the O–Cu–C angle is *ca.* 15° (**Cu1**) or 22° (**Cu2**) smaller than the N–Cu–C angle; this difference likely arises from the NHC tilting away from the more sterically encumbered side of the N^O ligand. The C–Cu bond distances are within the range of previously reported NHC–Cu(I) complexes.[34,35]

Frontier molecular orbitals

The frontier molecular orbitals of the stated Cu(I) complexes were computed *via* DFT, using the PBE0 hybrid functional and the D3BJ dispersion correction. To expedite computation, the NHC isopropyl groups were truncated to methyl groups; the truncated structures are denoted as **Cu1′** and **Cu2′**. The optimized geometries overlay well with the crystallographically determined structures (Fig. S51 and S52), indicating that the substituent modification does not drastically alter the preferred coordination geometry or ligand conformations. Selected molecular orbitals are presented in Fig. 2, with partial Kohn–Sham orbital energy-level diagrams in Fig. S53 and S54. The HOMO and LUMO of **Cu1′** both predominantly localize on the 8-hydroxyquinolinato ligand (97% contribution) with a minimal contribution (2.6%) from orbitals on copper. The electron density in the HOMO is more skewed towards the hydroxy-substituted ring, whereas the LUMO density shifts towards the N-heterocycle. The HOMO−1 is more delocalized, with significant copper character (60%) and moderate ligand character (10% NHC, 30% N^O). Similar orbital compositions are observed in **Cu2′** as well. These observations deviate somewhat from the previous literature report of $[Cu(N^N)(NHC)]^+$ complexes, in which metal-centered orbitals are major contributors to the HOMO.[34] We propose that the electron-rich nature of the anionic N^O ligands results in them being stronger contributors to the HOMO for both **Cu1′** and **Cu2′**. The computed HOMO–LUMO gaps are 3.73 eV in **Cu1′** and 3.58 eV in **Cu2′**.

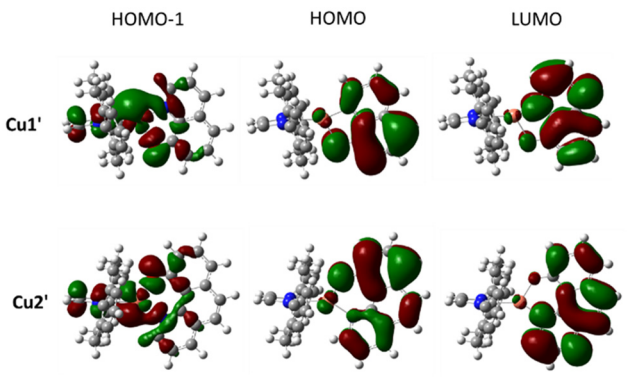

Fig. 2 Frontier molecular orbitals of **Cu1′** and **Cu2′**, computed *via* DFT, using the PBE0 hybrid functional and the D3BJ dispersion correction. The isopropyl groups of the NHC are truncated to methyl groups.

Photophysical properties

UV–vis absorption and steady-state photoluminescence spectra were measured in THF at room temperature (298 K), and photoluminescence spectra at 77 K were measured in 2-methyltetrahydrofuran. The overlaid spectra of **Cu1** and **Cu2** are depicted in Fig. 3 and all photophysical data are summar-

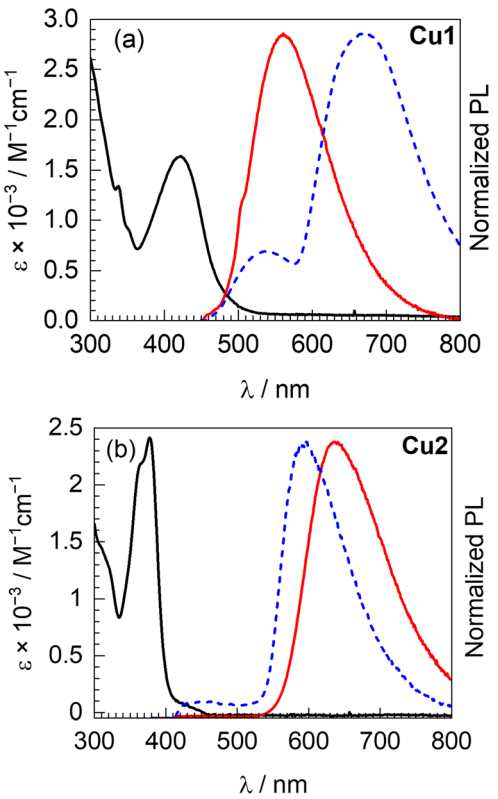

Fig. 3 UV–vis absorption and photoluminescence spectra (at 298 K and 77 K) of (a) **Cu1** and (b) **Cu2**, recorded in THF at room temperature and in 2-methyltetrahydrofuran at 77 K. Black solid line: absorption spectrum; red solid line: photoluminescence spectrum at 298 K; blue dashed line: photoluminescence spectrum at 77 K. The photoluminescence spectra are intensity-matched to the absorption spectrum at the long wavelength maximum.

ized in Table 1. Excitation spectra of these compounds, overlaid with their UV–vis absorption spectra, are presented in the SI (Fig. S1 and S2).

The UV–vis absorption spectra all exhibit a discernible band in the near-UV to visible region. More specifically, the spectrum of **Cu1** shows a maximum at 423 nm ($\varepsilon = 1.5 \times 10^3$ M^{-1} cm^{-1}, Fig. 3a, black solid line). On the other hand, in **Cu2** the main band has a maximum of 377 nm ($\varepsilon = 2.4 \times 10^3$ M^{-1} cm^{-1}, Fig. 3b, black solid line) with a weaker shoulder at 430 nm. To understand the nature of these visible transitions, time-dependent DFT analysis was performed on truncated model complexes **Cu1′** and **Cu2′**. The results are summarized in Tables S5 and S6 with simulated absorption spectra in Fig. S55 and S57, and they show that in each complex there is a low-energy singlet transition with substantial oscillator strength that is a pure HOMO → LUMO excitation. In **Cu2′** the computed S_1 state is a HOMO−1 → LUMO MLCT state, but its oscillator strength is negligible ($f = 0.0003$). Given the nature of the frontier orbitals described above, the most intense absorption transitions can be described as intra-ligand charge-transfer (^{1}ILCT) in both **Cu1** and **Cu2**. Electron–hole analysis, summarized pictorially in Fig. S56 (**Cu1′**) and Fig. S58 (**Cu2′**) confirm this assignment. In both cases, the more intense low-energy transition, S_1 in **Cu1′** and S_2 in **Cu2′**, has its excited-state hole distribution primarily on the hydroxy-substituted arm of the chelating ligand, with the electron distribution more delocalized but skewed towards the N-heterocycle ring.

The room-temperature photoluminescence of **Cu1** (Fig. 3, red solid lines) consists of a band with a maximum at 560 nm. The broad, featureless nature of this band, insights into the frontier orbitals and excited states from DFT and TD-DFT calculations, and the long excited-state lifetime (see below) are all consistent with phosphorescence originating from a triplet charge-transfer excited state. As further confirmation, electron–hole analysis of the $S_0 \rightarrow T_1$ transition of truncated model complex **Cu1′** (Fig. S56) shows that both the electron and hole distribute almost exclusively on the 8-hydroxyquinolato ligand, with the higher-lying T_2 level presenting as an MLCT state. The photoluminescence quantum yield (Φ_{PL}) is 0.03. The photoluminescence of **Cu1** at 77 K shows two bands: (i) a lower-intensity band at 535 nm, consistent with the rigidochromic shift of the room-temperature band; (ii) a more intense, low-energy band at 672 nm (Fig. 3a, blue dashed line). Such dual emission at 77 K is reproducible across multiple samples and concentrations, confirming it is intrinsic to the complex. The consistent appearance of this secondary band, along with the relative peak intensities being unaffected by concentration, effectively rules out excimer or aggregate emission as its source (Fig. S5). This temperature-dependent dual emission is most plausibly attributed to two closely spaced triplet excited states. At room temperature, thermal population favours emission from the higher-energy ^{3}CT state, resulting in the single emission band, whereas at 77 K, emission from the lower-energy triplet manifold becomes dominant, giving rise to the second intense band. This assumption was further supported by the lifetime analysis of **Cu1** at room temperature which is described in the following section.

At 298 K, **Cu2** shows bright red photoluminescence with its spectrum centered at 636 nm (Fig. 3b, black solid line), Φ_{PL} = 0.08. A significant hypsochromic shift of 43 nm (1100 cm^{-1}) was observed in the PL spectrum recorded at 77 K, in which the maximum occurs at 593 nm, (Fig. 3b, blue dashed line), likewise consistent with a charge-transfer transition. Similar to **Cu1**, the TD-DFT-computed $S_0 \rightarrow T_1$ transition and associated electron–hole analysis (Fig. S58) indicate that the low-energy triplet state in **Cu2** is best described as a ^{3}ILCT state. Consistent with the ligand-localized nature of the T_1 state, the T_1 geometries of **Cu1′** and **Cu2′**, optimized by spin-unrestricted DFT, are minimally different than those of the respective S_0 ground state (Fig. S59 and S60).

The PL lifetimes of **Cu1** and **Cu2** were determined by time-correlated single photon counting (TCSPC) in THF at room temperature, and the time-resolved photoluminescence decay traces are presented in Fig. S3 and S4. The observed lifetimes depend substantially on the choice of N^O ligand. The PL for **Cu1** decays on the microsecond timescale consistent with phosphorescence from a triplet excited state. The decay is best fit by a biexponential function, yielding τ_1 = 3.6 μs (minor, 6%) and τ_2 = 46 μs (major, 94%), corresponding to an average lifetime τ_{avg} = 44 μs. No prompt (nanosecond-scale) component was detected, confirming that the observed photoluminescence is attributed exclusively to phosphorescence rather than fluorescence. This observation supports the presence of two emissive triplet decay pathways in **Cu1**, either originating from two closely spaced and non-interconverting triplet excited states or two conformationally distinct environments. Consistent with this interpretation, a dual-emission profile is observed at 77 K. On the other hand, the excited state lifetime is over an order of magnitude smaller in **Cu2** (2.9 μs), reflecting a faster deactivation of its triplet excited state compared to **Cu1**. In combination with the observed photoluminescence quantum yields, we find that the radiative rate constant in **Cu2** ($k_r = 3 \times 10^4$ s^{-1}) is over 40× larger than that of **Cu1** ($k_r = 7 \times 10^2$ s^{-1}), with the nonradiative rate constants also

Table 1 Summary of photophysical data of **Cu1** and **Cu2**

	UV–vis absorption, λ/nm ($\varepsilon \times 10^{-3}$/$M^{-1}$ cm^{-1})	PL, 298 K, λ/nm	PL, 77 K, λ/nm	τ/μs	Φ_{PL}	k_r/s^{-1}	k_{nr}/s^{-1}	$E_{0,0}$[a]/eV
Cu1	338 (1.3), 423 (1.6)	560	535, 672	44	0.03	7×10^2	2×10^4	2.3
Cu2	365 (2.2), 377 (2.4), 430 (0.64)	636	593	2.9	0.08	3×10^4	3×10^5	2.1

[a] $E_{0,0}$ value were calculated from the $\lambda_{0,0}$ peak in the 77 K emission spectra.

exhibiting an order-of-magnitude difference (2×10^4 s^{-1} in **Cu1** and 3×10^5 s^{-1} in **Cu2**).

Electrochemistry

The electrochemical properties of **Cu1** and **Cu2** were analyzed by cyclic voltammetry, and the resulting voltammograms are depicted in Fig. 4. The results of electrochemical analysis are summarized in Table 2. All reduction potentials are reported relative to the ferrocenium/ferrocene (Fc^+/Fc^0) redox couple as the internal reference. The wave associated with the one-electron oxidation of both **Cu1** and **Cu2** is reversible in nature, with $E_{1/2}$ values of 0.35 V and 0.28 V, respectively (Fig. 4). **Cu1** possesses two irreversible reduction waves, at −2.59 V and −2.78 V, respectively. On the other hand, **Cu2** shows an irreversible reduction wave at −2.56 V. The reduction is expected to involve the LUMO, which is primarily localized on the quinoline or benzoquinoline ring (Fig. 2). The excited-state oxidation potentials ($*E^{ox}$) for these complexes, *i.e.*, the redox potentials associated with electron transfer from the excited state, were estimated and presented in Table 2. **Cu1** has a more negative $*E^{ox}$ (−2.0 V) compared to **Cu2** ($*E^{ox}$ = −1.8 V), signifying it is a slightly stronger photoreductant.

Photocatalytic activity

The excited-state redox potentials of **Cu1** and **Cu2**, combined with their long excited-state lifetimes, suggest they could be potent photoredox reagents. Defined as $E([Cu]^+/*[Cu])$, the estimated $*E^{ox}$ values of these compounds (Table 2) are −2.0 and −1.8 V, respectively, indicating they are strong photoreductants. Therefore, we chose to check the photocatalytic ability of these two complexes in reductive transformations of organic compounds. As a model reaction, we chose the photo-hydrogenation of different substituted benzophenone substrates, a reaction we have previously studied using iridium photosensitizers[37] and β-diketiminate (NacNac)-supported copper(I) photosensitizers.[38,39] The reaction conditions are depicted in Scheme 2. 4-Cyanobenzophenone (**S1**) was selected as the initial test substrate and 1,3-dimethyl-2-phenyl-2,3-dihydro-1*H*-benzo[d]imidazole (BIH) was chosen as a sacrificial electron and hydrogen donor. The catalytic reactions were carried out in an NMR tube with **S1** (1 equiv.), BIH (2 equiv.) and the copper catalyst (**Cu1** or **Cu2**, 10 mol%), in the presence of an internal integration standard (1,3,5-trimethoxybenzene) in C_6D_6. Samples were irradiated with blue LEDs and monitored by ^1H NMR spectra recorded at different time intervals. Within 10 h, we determined a 99% NMR yield of the desired hydrogenated product (4-cyanobenzhydrol, **P1**) with both **Cu1** and **Cu2** as the photosensitizer. A control reaction without any copper catalyst, otherwise identical, resulted in no product formation. We then moved to check the scope of various benzophenone substrates containing electron-donating or electron-withdrawing groups.

NMR spectra for these screens are presented in the SI (Fig. S12–S28). The yields of all catalytic reactions were determined *via* integration of the NMR spectrum relative to the internal standard. In two cases (unsubstituted **S2** and dicyano-

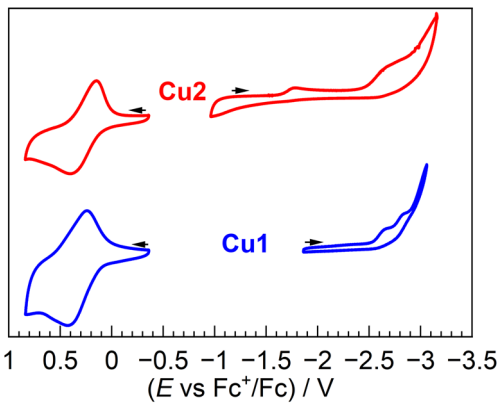

Fig. 4 Overlaid cyclic voltammograms of **Cu1** and **Cu2**, recorded in THF with 0.1 M NBu_4PF_6 electrolyte, using a glassy carbon working electrode, platinum wire counter electrode, and silver wire pseudo-reference electrode. A scan rate 0.1 V s^{-1} was used, and potentials are reported relative to an internal standard of ferrocene.

Table 2 Summary of electrochemical data of **Cu1** and **Cu2**

	E^{ox}/V^a ($[Cu]^+/[Cu]^0$)	E^{red}/V^a ($[Cu]^0/[Cu]^-$)	$*E^{ox}/V^b$ ($[Cu]^+/*[Cu]^0$)
Cu1	0.35	−2.59, −2.78	−2.0
Cu2	0.28	−1.70, −2.56	−1.8

[a] Potentials for reversible couples are reported as half-wave potentials ($E_{1/2}$), whereas for irreversible couples half-peak potentials[36] are given. [b] Estimated as $E^{ox} - E_{0,0}$ (see Table 1 for $E_{0,0}$ values).

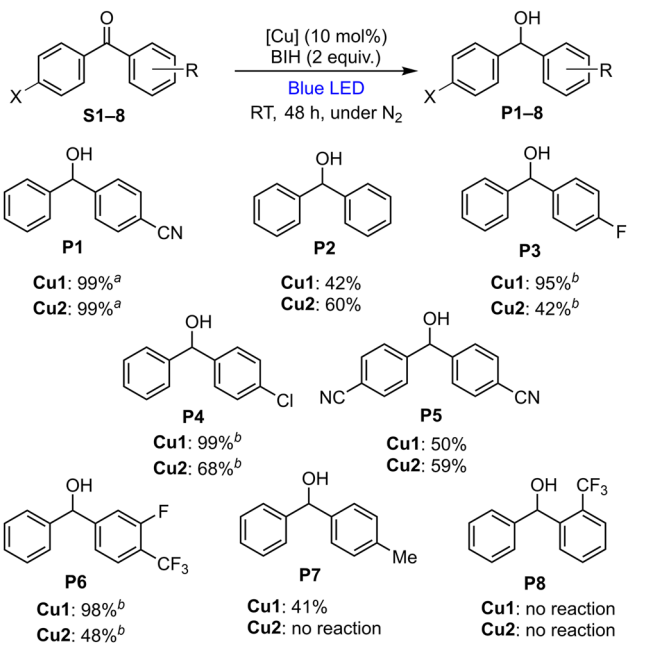

Scheme 2 Photocatalytic hydrogenation of benzophenones using **Cu1** and **Cu2** as photocatalysts. NMR yields for all products were determined using 1,3,5-trimethoxybenzene as internal standard. [a] Reaction time 10 h. [b] Reaction time 24 h.

substituted **S5**) both photosensitizers produce modest and similar yields of the hydrogenation product; the latter example is curious since **S5** should be the most activated substrate. For a few of the halo-substituted examples (**S3**, **S4**, and **S6**), **Cu1** clearly performs better as a photosensitizer and gives near-quantitative yield of the respective benzhydrol product, with only modest yields obtainable with **Cu2**. Methyl-substituted **S7** is the most difficult substrate to reduce in this series, and we were only able to obtain significant amounts of hydrogenation product (41%) with **Cu1**. Finally, with **S8** no productive reaction was observed with either catalyst, which we tentatively ascribe the sterically blocking nature of the 2-trifluoromethyl substituent. Overall, **Cu1** outperforms **Cu2** as a photocatalyst, which is likely a function of it being a stronger photoreductant ($^*E^{ox}$ −2.0 V *vs.* −1.8 V) and having a longer excited-state lifetime, both of which can contribute to higher quantum yields for photoinduced electron transfer to the substrate.

Similar photoredox transformations were previously carried out using a cyclometalated iridium photocatalyst.[37] The previous work used 1 mol% catalyst (instead of 10 mol% as used herein), with otherwise identical conditions. The yields with **Cu1** are comparable to or exceed those obtained with the Ir photocatalyst in reactions involving the activated substrates (those with electron-withdrawing groups, **S1**, **S3**, and **S4**). Interestingly, with **Cu1**, photoreduction of **S4** exhibits high selectivity for hydrogenation (**P4**) over hydrodechlorination, whereas the previously described Ir catalyst also produced a substantial amount of **P2** *via* combined hydrogenation and hydrodechlorination.[37] However, the present Cu photocatalysts fall well short of the Ir photocatalyst with substrates bearing electron-donating substituents due to their comparatively lower excited-state reducing power compared to the Ir catalyst.

To determine kinetically preferred photoinduced electron transfer steps in the above-described photoredox reactions, Stern–Volmer quenching experiments were performed with both **Cu1** and **Cu2** using 4-cyanobenzophenone (**S1**), benzophenone (**S2**), and BIH as quenchers. The data for the quenching experiments are presented in Fig. S6–S11 and summarized in Table S4. With **Cu1**, the quenching rate constants of **S1** (k_q = 6.2 × 10^7 M^{-1} s^{-1}) and **S2** (k_q = 5.9 × 10^6 M^{-1} s^{-1}) are significantly higher than that of BIH (k_q = 5.2 × 10^5 M^{-1} s^{-1}), suggesting oxidative quenching with the benzophenone substrates is much faster than reductive quenching by BIH. Similar observations were made with **Cu2**: the quenching rate constants of **S1** (k_q = 2.6 × 10^7 M^{-1} s^{-1}) and **S2** (k_q = 3.1 × 10^7 M^{-1} s^{-1}) are much faster than BIH (k_q = 2.7 × 10^6 M^{-1} s^{-1}), signifying that oxidative quenching by the substrate is kinetically favored.

As a second class of challenging organic substrates, we were also interested to see if **Cu1** and **Cu2** could reductively activate organohalide substrates. Scheme 3 summarizes hydro-dehalogenation reactions of aryl halide and benzyl halide substrates, with the associated ^{1}H NMR spectra presented in the SI (Fig. S29–S44). Reaction conditions were very similar to those of the photo-hydrogenation reactions, with the substrate, BIH (2 equiv.), and photosensitizer (10 mol%) irradiated with blue

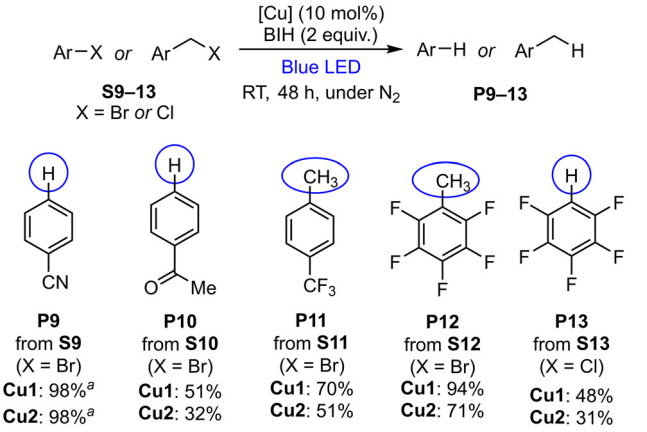

Scheme 3 Photocatalytic de-halogenation of aryl/alkyl halides using **Cu1** and **Cu2** as photocatalysts. NMR yields for all products were determined using 1,3,5-trimethoxybenzene or hexafluorobenzene as internal standard. [a] Reaction time 24 h.

LED light in C_6D_6 with an internal standard (1,3,5-trimethoxybenzene). With 4-bromobenzonitrile (**S9**), a 98% NMR yield of the respective hydrodebrominated product benzonitrile (**P9**) was recorded after 24 h, using both copper catalysts. Methyl-4-bromobenzoate (**S10**) is reduced to the product methyl benzoate (**P10**) in moderate yields, 51% with **Cu1** and only 32% yield using **Cu2**, after 48 h. Benzyl bromide substrates are well-tolerated, with 1-methyl-4-(trifluoromethyl)benzene (**P11**) and pentafluorotoluene (**P12**) produced from the respective benzyl bromide substrates in 70% and 94% yield, respectively, using **Cu1** as the photocatalyst. However, considerably low yields were recorded with **Cu2**, *i.e.* 51% and 71%, respectively. Finally, we tested the catalysts' ability to activate the C–Cl bond in chloropentafluorobenzene (S13). Moderate yields were observed after 48 h of irradiation; 48% with **Cu1**, and 31% for **Cu2**.

Given the long excited-state lifetimes and relatively high triplet energies of **Cu1** and **Cu2** (see Table 1), we further investigated the photocatalytic activity of these compounds in a reaction involving triplet–triplet energy transfer. The isomerization of (*E*)-stilbene (1 equiv.) occurs in the presence of **Cu1** or **Cu2** (10 mol%) under blue-light irradiation. Again, the reactions were carried out in an NMR tube using C_6D_6 as the solvent and 1,3,5-trimethoxybenzene as the internal standard (Fig. S45 and S46). A summary of the isomerization progression is presented in Table 3. In both cases, the photostationary *E* : *Z* ratio was nearly reached within 1 hour of irradiation, with only slight additional progression over the next 23 hours. The two photosensitizers gave quite different photostationary states, with **Cu2** nearly completely isomerizing the (*E*)-stilbene; the final *E* : *Z* ratio after 24 h is 8 : 91 (Table 3, entry 4). However, in spite of its much longer excited-state lifetime, **Cu1** resulted in less isomerization, and after 24 hours of irradiation a 61 : 39 *E* : *Z* ratio was observed (Table 3, entry 2). We attribute these differences to the slightly different triplet excited-state energies of the two photosensitizers. The triplet

Table 3 Photocatalytic *E*/*Z* isomerization of (*E*)-stilbene: triplet–triplet energy transfer using Cu(I)–NHC complexes as photocatalysts

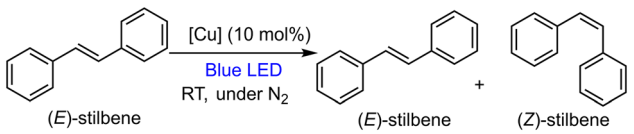

Entry	Catalyst	Time/h	*E* : *Z*
1	**Cu1**	1	68 : 32
2	**Cu1**	24	61 : 39
3	**Cu2**	1	16 : 84
4	**Cu2**	24	8 : 91
5[a]	**Cu1**	24	100 : 1
6[a]	**Cu2**	24	100 : 1
7[b]	—	24	100 : 1

[a] Catalytic reactions performed in dark (without blue LED irradiation) for 24 h. [b] Reaction performed in the absence of copper photosensitizer.

energy of (*E*)-stilbene is 2.14 eV and that of (*Z*)-stilbene is 2.57 eV,[40] and we estimate that the triplet excited-state energy of **Cu1** is *ca.* 0.2 eV higher than that of **Cu2** (Table 1), which may allow **Cu1** to back-sensitize (*Z*)-stilbene and limit the conversion ratio. Control experiments reveal no isomerization in the dark (Table 3, entries 5 and 6) or when the alkene is irradiated in the absence of a copper photosensitizer (Table 3, entry 7). The catalytic outcomes described here are comparable with our previous report of Cu(I)(NacNac)(ArNC) series of complexes,[38,39] as well as a recent report that uses a cationic Cu(I)–phenanthroline–NHC complex.[41] These results demonstrate that these three-coordinate Cu(I) photosensitizers can promote some of the same reactions that were originally developed with noble-metal photocatalysts. Compared with typical organic photocatalysts, **Cu1** and **Cu2** offer stronger excited-state reducing power and longer triplet lifetimes, underscoring their potential as sustainable photoredox platforms. Overall, this present study introduces a modular class of three-coordinate Cu(I) photosensitizers featuring ligand-localized frontier orbitals, enabling long-lived excited states and potent photoreductive capabilities for versatile applicability in photocatalysis.

Conclusions

In summary, herein we report a complimentary class of Cu(I) NHC complexes featuring quinoline-based chelating N^O-ligands. Both of the reported Cu(I) complexes, **Cu1** and **Cu2**, have all of the desirable attributes for a photosensitizer—intense visible absorption, long excited-state lifetimes (as high as 44 μs), and potent excited-state redox reactivity, allowing them to function in photocatalytic reactions. A combination of electrochemical and photophysical measurements, supplemented with DFT calculations, reveals one key distinction of this design compared to other heterolpetic copper(I) photosensitizers. In the compounds introduced here, both the HOMO and LUMO are localized on the same ligand, unlike typical heteroleptic designs that spatially separate the two frontier orbitals. As such, the low-energy charge-transfer transitions that occur almost exclusively involve the N^O ligand, and structural modifications to this ligand effectively tune redox potentials, HOMO–LUMO gaps, and photoluminescence properties. The NHC is photophysically innocent, but nonetheless its strong donor abilities and significant steric bulk are likely important in stabilizing the three-coordinate structure and inhibiting the well-known excited-state distortions that deactivate charge-transfer excited states in copper(I) complexes. These results motivate studies of copper(I) and other earth-abundant charge-transfer chromophores supported by related classes of chelating ligands that partner an electron-rich anionic donor with a π-accepting conjugated group.

Experimental section

Materials and methods

All reactions were performed in a nitrogen-filled glovebox (at <1 ppm of oxygen and <1 ppm of H_2O). Solvents for synthesis, photophysical and electrochemical measurements were either dried and deoxygenated in a solvent purification system and stored over 3 Å molecular sieves or were obtained commercially at anhydrous grade and used directly. NMR solvents were stored inside the glovebox over 3 Å molecular sieves. ^{1}H, $^{13}C\{^{1}H\}$ and ^{19}F NMR spectra were recorded on a JEOL ECA-400 or JEOL ECA-500 NMR spectrometer at room temperature. High-resolution mass spectrometry (HRMS) was performed at the University of Houston Mass Spectrometry Laboratory using an Agilent 6546 qTOF mass spectrometer. Samples for HRMS were prepared in LC/MS-grade MeCN. Stock solutions for photophysical measurements were prepared inside a nitrogen-filled glovebox using anhydrous solvents. UV–vis absorption spectra were recorded in anhydrous solvent in a screw-capped quartz cuvettes using an Agilent Cary 8454 UV–vis spectrometer. Steady-state photoluminescence and excitation spectra were recorded using a Horiba FluoroMax-4 spectrofluorometer. The data are corrected for detector response and excitation intensity. Low-temperature photoluminescence measurements were performed in a custom quartz EPR tube with high-vacuum valve, which was immersed in a sample holder consisting of a finger Dewar filled with liquid nitrogen to attain a temperature of 77 K. Solution-state photoluminescence measurements were performed in quartz cuvettes with 1.0 cm path length, using solutions with concentrations adjusted to give absorbance values of 0.05–0.2 at the excitation wavelength.

Photoluminescence quantum yields were determined relative to a standard of tetraphenylporphyrin (TPP) in toluene which has a reported fluorescence quantum yield of 0.11, or quinine sulfate in 0.05 M aqueous sulfuric acid which has a reported fluorescence quantum yield of 0.52.[42,43] For the standard and each sample, five optically dilute samples of varying concentrations were measured, prepared by sequential addition of a stock solution to toluene in a screw-capped

cuvette. The absorbance at the excitation wavelength was <0.1 for each measurement. UV–vis absorption spectra and a PL spectrum was recorded at each concentration, ensuring identical slit widths for each measurement. The PL spectrum was integrated using OriginPro software, and for the copper complex and the standard the integrated PL was plotted *vs.* the absorbance at the excitation wavelength, which for optically dilute samples yields a straight line. The slope of each line was determined, and by using eqn (1) below the quantum yield was determined: Φ_x is the PL quantum yield of the copper complex and Φ_{st} is the quantum yield of the standard. A correction for solvent index of refraction was not needed, since toluene was used as the solvent for both the standard and the copper complex.

$$\Phi_x = \Phi_{st} \frac{\text{slope}_x}{\text{slope}_{st}} \quad (1)$$

Photoluminescence lifetimes of the copper complexes were measured on a Horiba DeltaFlex Lifetime system using a 460 nm or 390 nm pulsed diode excitation source. Cyclic voltammetry (CV) measurements were performed with a CH instrument 602E potentiostat interfaced with a nitrogen-filled glovebox *via* wire feedthroughs. Tetrabutylammonium hexafluorophosphate (NBu_4PF_6) was used as the supporting electrolyte (0.1 M solution in THF), glassy carbon (3 mm diameter) was used as the working electrode, Pt wire was the counter electrode, and a silver wire immersed in 0.1 M NBu_4PF_6 THF solution was used as a pseudo-reference electrode. CV measurements were referenced to an internal standard ferrocene. Starting materials and reagents were obtained from commercial sources unless otherwise stated. Benzyl potassium[44] and 1,3-dimethyl-2-phenyl-2,3-dihydro-1*H*-benzo[d]imidazole (BIH)[45] were prepared by following reported procedures.

General procedure for preparation of N^O–K and N^O–Na salts

In a nitrogen filled glovebox, the neutral N^O–H proligand (8-hydroxyquinoline, **L1H** or 10-hydroxybenzo[h]quinoline, **L2H**, 1 mmol) was added to a 20 mL vial equipped with a stir bar. Benzylpotassium (for **L1H**, 1 mmol) or NaHMDS (for **L2H**, 1 mmol) was added to the reaction pot followed by the addition of diethyl ether (5 mL). The reaction mixture was stirred at room temperature for 12 hours. After completion, a yellowish precipitate was observed. The supernatant was decanted and rest of the reaction mixture was dried under vacuum to obtain yellow solid product.

General procedure for preparation of the Cu complexes

In a nitrogen-filled glovebox, **L1-K** or **L2-Na** (0.2 mmol) was added to a 20 mL vial equipped with a stir bar. Anhydrous THF (10 mL) was added, and the mixture was stirred for 15 minutes to make a clear solution. In a separate vial, (2,5-bis (2,6-diisopropylphenyl)cyclopent-3-en-1-yl)copper(II) chloride (IPr–Cu–Cl, 1.2 equiv., 0.24 mmol) was dissolved in THF, and this solution was added dropwise to the reaction vial containing the N^O ligand. The reaction mixture was allowed to stir for 24 hours at room temperature. After completion, THF was evaporated under vacuum, followed by a two-step extraction of the compound into toluene. The crude product was purified by washing with pentane. Both Cu complexes were characterized by ^{1}H and $^{13}C\{^1H\}$ NMR spectroscopy and X-ray crystallography.

Synthesis of L1–Cu–IPr (Cu1). Cu1 was prepared by using IPr–Cu–Cl (0.209 mmol, 102 mg) and **L1-K** (0.17 mmol, 32 mg) following the general synthetic procedure. The crude compound was purified by repeated washing with pentane (3 times). Yield: 72 mg, 69%. Yellow block-shaped single crystals of this compound were grown from a THF solution layered with pentane inside the glovebox freezer. ^{1}H NMR (500 MHz, C_6D_6) δ (ppm): 7.52 (dd, J_1 = 8.5 Hz, J_2 = 1.5 Hz, 1H, C$\underline{H}^{Ar}$), 7.42 (br, d, J = 4.0 Hz, 1H, C$\underline{H}^{Ar}$), 7.33 (t, J = 7.8 Hz, 1H, C$\underline{H}^{Ar}$), 7.21–7.18 (m, 3H, C$\underline{H}^{Ar/NHC}$), 7.10 (d, J = 7.5 Hz, 4H, C$\underline{H}^{NHC}$), 6.65 (dd, J_1 = 8.0 Hz, J_2 = 4.5 Hz, 1H, C$\underline{H}^{Ar}$), 6.58 (dd, J_1 = 8.0 Hz, J_2 = 1.0 Hz, 1H, C$\underline{H}^{Ar}$), 6.41 (s, 2H, C$\underline{H}^{NHC}$), 2.89 (sept, J = 6.8 Hz, 4H, iPr C$\underline{H}^{NHC}$), 1.44 (d, J = 7.0 Hz, 12H, iPr C$\underline{H}_3^{NHC}$), 1.13 (d, J = 7.0 Hz, 12H, iPr C$\underline{H}_3^{NHC}$). $^{13}C\{^1H\}$ NMR (126 MHz, C_6D_6) δ (ppm): 187.1(N$\underline{C}$N), 146.1, 143.71, 143.68, 137.1, 136.4, 130.9, 130.8, 130.1, 128.3, 124.2, 122.0, 119.5, 113.4, 106.6, 29.0 ($\underline{C}$H), 24.7 ($\underline{C}H_3$), 24.0 ($\underline{C}H_3$).

Synthesis of L2–Cu–IPr (Cu2). Cu2 was prepared by using IPr–Cu–Cl (0.16 mmol, 80 mg) and **L2-Na** (0.14 mmol, 31 mg) following the general synthetic procedure. The crude compound was purified by repeated washing with pentane (3 times). Yield: 66 mg, 73%. Red plate-shaped single crystals of this compound were grown from toluene solution layered with pentane inside the glovebox freezer. ^{1}H NMR (500 MHz, C_6D_6) δ (ppm): 7.81 (dd, J_1 = 5.0 Hz, J_2 = 2.0 Hz, 1H, C$\underline{H}^{Ar}$), 7.60 (t, J = 7.8 Hz, 1H, C$\underline{H}^{Ar}$), 7.45 (d, J = 8.5 Hz, 1H, C$\underline{H}^{Ar}$), 7.33 (dd, J_1 = 8.0 Hz, J_2 = 2.0 Hz, 1H, C$\underline{H}^{Ar}$), 7.27 (d, J = 7.0 Hz, 1H, C$\underline{H}^{Ar}$), 7.22 (t, J = 7.8 Hz, 2H, C$\underline{H}^{NHC}$), 7.14–7.10 (m, 4H, C$\underline{H}^{NHC}$), 6.90 (d, J = 5.5 Hz, 1H, C$\underline{H}^{Ar}$), 6.85 (d, J = 7.0 Hz, 1H, C$\underline{H}^{Ar}$), 6.57 (dd, J_1 = 8.0 Hz, J_2 = 5.0 Hz, 1H, C$\underline{H}^{Ar}$), 6.46 (br s, 2H, C$\underline{H}^{NHC}$), 2.95 (br s, 4H, iPr C$\underline{H}^{NHC}$), 1.41 (d, J = 7.0 Hz, 12H, iPr C$\underline{H}_3^{NHC}$), 1.13 (d, J = 7.0 Hz, 12H, iPr C$\underline{H}_3^{NHC}$). $^{13}C\{^1H\}$ NMR (126 MHz, C_6D_6) δ (ppm): 171.9(N$\underline{C}$N), 149.9, 149.0, 146.2, 137.9, 135.3, 131.8, 130.5, 129.3, 128.3, 127.4, 124.1, 123.2, 121.9, 121.4, 118.3, 116.5, 110.7, 28.9 ($\underline{C}$H), 24.5 ($\underline{C}H_3$), 24.2 ($\underline{C}H_3$).

X-ray crystallography

Single crystals of both copper complexes were mounted on a Bruker Apex II three-circle diffractometer using MoKα radiation (λ = 0.71073 Å). The data were collected at 123(2) K and processed and refined within the APEXII software. Structures were solved by intrinsic phasing in SHELXT and refined by standard difference Fourier techniques in the program SHELXL.[46] Hydrogen atoms were placed in calculated positions using the standard riding model and refined isotopically; all non-hydrogen atoms were refined anisotropically.

Photocatalysis

Photocatalytic reactions were carried out using a home-built photoreactor that consists of a glass dish wrapped with blue LED strips (purchased from Creative Lighting Solutions, Model: Blue Flexible LED Strips, 12 vdc. Emission profile: 400–500 nm) on the inside wall with the outside wall wrapped with aluminum foil.

Hydrogenation of benzophenone substrates. In a nitrogen-filled glovebox, the respective benzophenone substrate (**S1–S8**, 0.05 mmol), BIH (0.1 mmol) as a sacrificial reagent and hydrogen source, and 1,3,5-trimethoxybenzene (0.017 mmol, 0.33 equiv.) as an internal standard were taken in a small vial and dissolved in 0.7 mL of C_6D_6. The copper photosensitizer (10 mol%) was added to it, then the mixture was transferred to an NMR tube which was further sealed with parafilm and taken out of glovebox. The NMR tube was placed inside the photoreactor and irradiated with blue LED light. The NMR yield of the product was determined by ^{1}H NMR spectroscopy, integrating relative to the internal standard.

Hydrodehalogenation of aryl/alkyl halides. In a nitrogen-filled glovebox, the respective aryl/alkyl halide substrate (**S9–S13**, 0.05 mmol), BIH (0.1 mmol) as a sacrificial reagent and hydrogen source, and 1,3,5-trimethoxybenzene (0.017 mmol, 0.33 equiv.) as an internal standard were taken in a small vial and dissolved in 0.7 mL of C_6D_6. The copper photosensitizer (10 mol%) was added to it, then the mixture was transferred to an NMR tube which was further sealed with parafilm and taken out of glovebox. The NMR tube was placed inside the photoreactor and irradiated with blue LED light. The NMR yield of the product was determined by ^{1}H NMR spectroscopy, integrating relative to the internal standard.

***E*/*Z* isomerization of (*E*)-stilbene.** In a nitrogen-filled glovebox, (*E*)-stilbene (6.3 mg, 0.035 mmol), the copper photosensitizer (10 mol%) and 1,3,5-trimethoxybenzene (6 mg, 0.035 mmol) as an internal standard were taken in a small vial and dissolved in 0.7 mL of C_6D_6. The reaction mixture was transferred to an NMR tube which was further sealed with parafilm and taken out of glovebox. The NMR tube was placed inside the photoreactor and irradiated with blue LED light. For control reactions, a similar set up was made either (i) without using the catalyst; or (ii) the NMR tube was placed in dark for 24 h. All the reactions were monitored by ^{1}H NMR spectroscopy. The *E*/*Z* ratio was determined by ^{1}H NMR spectroscopy, integrating relative to the internal standard.

Stern–Volmer quenching experiments. In a nitrogen-filled glovebox, stock solutions of the copper photosensitizer (4 mg in 2.5 mL of toluene), 4-cyanobenzophenone (45 mg in 1.2 mL of toluene), benzophenone (50 mg in 1.2 mL of toluene) and BIH (60 mg in 0.8 mL of toluene) were prepared. The cuvette was filled with 2.5 mL of toluene and 10–15 μL of the stock solution of the copper complex. The photoluminescence spectrum was recorded in the absence of quencher and after each addition of different aliquots of the quencher solution. The ratio (I_0/I), where I_0 and I are the photoluminescence intensity in the absence and presence of quencher, respectively, was plotted against concentration of the quencher to determine the Stern–Volmer constant (K_{SV}) directly from the slope. The quenching rate constant (k_q) is related to K_{SV} as follows: $K_{SV} = k_q \times \tau_0$, where τ_0 is the photoluminescence lifetime of the copper complex.

DFT calculations

Density functional theory (DFT) computations were carried out using Gaussian16[47] to model the frontier orbitals and excited states of the luminescent copper complexes **Cu1** and **Cu2**. For each compound, the molecular geometry from single-crystal X-ray diffraction was used as the input and the isopropyl groups on the NHC ligand were truncated to methyl groups. Ground state geometries were optimized, and frequency analysis reported no imaginary frequency, thereby confirming the converged structures to be minima of the potential energy hypersurface. The first 20 singlet and triplet excited states were calculated by time-dependent DFT (TD-DFT) on the ground state geometries (Franck–Condon excited states). The PBE0 hybrid functional[48] and the D3BJ dispersion correction[49,50] was applied throughout. The SDD core potential and basis set[51] were utilized for copper, while the TZVP basis sets[52] were assigned to nonmetal atoms. Electron–hole analysis[53] on excited-state transitions was performed with Multiwfn,[54] and the plots were prepared using Blender 4.5.[55]

Author contributions

Soumi Chakraborty: conceptualization, formal analysis, investigation, validation, visualization, writing – original draft preparation, writing – review & editing. Erqian Mao: formal analysis, investigation, visualization, writing – review & editing. Thomas G. Gray: funding acquisition, supervision, writing – review & editing. Thomas S. Teets: conceptualization, funding acquisition, project administration, supervision, visualization, writing – review & editing.

Conflicts of interest

There are no conflicts to declare.

Data availability

The datasets supporting this article have been uploaded as part of the supplementary information (SI). Supplementary information: experimental details, X-ray crystallography summary, additional electrochemical and photophysical data, NMR spectra, and summaries of DFT calculations. DFT-optimized Cartesian coordinates in .xyz format. See DOI: https://doi.org/10.1039/d5dt02991k.

CCDC 2418726 and 2418727 contain the supplementary crystallographic data for this paper.[56a,b]

Acknowledgements

The work at the University of Houston was supported by the U. S. Department of Energy (DOE), Office of Science, Office of Basic Energy Sciences, CSGB Division under Award No. DE-SC0023394. Theoretical calculations at CWRU were supported by the Army Research Office, contract W911NF2510003 to T. G. G.

References

1 C. K. Prier, D. A. Rankic and D. W. C. MacMillan, *Chem. Rev.*, 2013, **113**, 5322–5363.
2 J. W. Beatty and C. R. J. Stephenson, *Acc. Chem. Res.*, 2015, **48**, 1474–1484.
3 T. C. Pham, V.-N. Nguyen, Y. Choi, S. Lee and J. Yoon, *Chem. Rev.*, 2021, **121**, 13454–13619.
4 X. Zhao, J. Liu, J. Fan, H. Chao and X. Peng, *Chem. Soc. Rev.*, 2021, **50**, 4185–4219.
5 J. Beaudelot, S. Oger, S. Peruško, T.-A. Phan, T. Teunens, C. Moucheron and G. Evano, *Chem. Rev.*, 2022, **122**, 16365–16609.
6 I. N. Mills, J. A. Porras and S. Bernhard, *Acc. Chem. Res.*, 2018, **51**, 352–364.
7 *Iridium(III) in Optoelectronic and Photonics Applications*, ed. E. Zysman-Colman, John Wiley & Sons, Inc, Chichester, West Sussex, 2017.
8 J. Zhao, W. Wu, J. Sun and S. Guo, *Chem. Soc. Rev.*, 2013, **42**, 5323.
9 M. Ankathatti Munegowda, A. Manalac, M. Weersink, S. A. McFarland and L. Lilge, *Coord. Chem. Rev.*, 2022, **470**, 214712.
10 S. Huo, J. Carroll and D. A. K. Vezzu, *Asian J. Org. Chem.*, 2015, **4**, 1210–1245.
11 M. Yoshida and M. Kato, *Coord. Chem. Rev.*, 2020, **408**, 213194.
12 H. Amouri, *Chem. Rev.*, 2023, **123**, 230–270.
13 F. N. Castellano and M. C. Rosko, *Acc. Chem. Res.*, 2024, **57**, 2872–2886.
14 M. S. Lazorski and F. N. Castellano, *Polyhedron*, 2014, **82**, 57–70.
15 R. Czerwieniec, M. J. Leitl, H. H. H. Homeier and H. Yersin, *Coord. Chem. Rev.*, 2016, **325**, 2–28.
16 H. Takeda, A. Kobayashi and K. Tsuge, *Coord. Chem. Rev.*, 2022, **470**, 214700.
17 M. Schulz, C. Reichardt, C. Müller, K. R. A. Schneider, J. Holste and B. Dietzek, *Inorg. Chem.*, 2017, **56**, 12978–12986.
18 M. Schulz, N. Hagmeyer, F. Wehmeyer, G. Lowe, M. Rosenkranz, B. Seidler, A. Popov, C. Streb, J. G. Vos and B. Dietzek, *J. Am. Chem. Soc.*, 2020, **142**, 15722–15728.
19 R. Hamze, J. L. Peltier, D. Sylvinson, M. Jung, J. Cardenas, R. Haiges, M. Soleilhavoup, R. Jazzar, P. I. Djurovich, G. Bertrand and M. E. Thompson, *Science*, 2019, **363**, 601–606.
20 S. Shi, M. C. Jung, C. Coburn, A. Tadle, D. Sylvinson M. R., P. I. Djurovich, S. R. Forrest and M. E. Thompson, *J. Am. Chem. Soc.*, 2019, **141**, 3576–3588.
21 C. N. Muniz, C. A. Archer, J. S. Applebaum, A. Alagaratnam, J. Schaab, P. I. Djurovich and M. E. Thompson, *J. Am. Chem. Soc.*, 2023, **145**, 13846–13857.
22 D. Kim, T. G. Gray and T. S. Teets, *Chem. Commun.*, 2022, **58**, 11446–11449.
23 V. A. Krylova, P. I. Djurovich, J. W. Aronson, R. Haiges, M. T. Whited and M. E. Thompson, *Organometallics*, 2012, **31**, 7983–7993.
24 A. Ruduss, B. Turovska, S. Belyakov, K. A. Stucere, A. Vembris and K. Traskovskis, *Inorg. Chem.*, 2022, **61**, 2174–2185.
25 J. Föller, C. Ganter, A. Steffen and C. M. Marian, *Inorg. Chem.*, 2019, **58**, 5446–5456.
26 V. A. Krylova, P. I. Djurovich, B. L. Conley, R. Haiges, M. T. Whited, T. J. Williams and M. E. Thompson, *Chem. Commun.*, 2014, **50**, 7176–7179.
27 A. Liske, L. Wallbaum, T. Hölzel, J. Föller, M. Gernert, B. Hupp, C. Ganter, C. M. Marian and A. Steffen, *Inorg. Chem.*, 2019, **58**, 5433–5445.
28 M. Gernert, L. Balles-Wolf, F. Kerner, U. Müller, A. Schmiedel, M. Holzapfel, C. M. Marian, J. Pflaum, C. Lambert and A. Steffen, *J. Am. Chem. Soc.*, 2020, **142**, 8897–8909.
29 S. Gaillard, C. S. J. Cazin and S. P. Nolan, *Acc. Chem. Res.*, 2012, **45**, 778–787.
30 R. Marion, F. Sguerra, F. Di Meo, E. Sauvageot, J.-F. Lohier, R. Daniellou, J.-L. Renaud, M. Linares, M. Hamel and S. Gaillard, *Inorg. Chem.*, 2014, **53**, 9181–9191.
31 R. Hamze, R. Jazzar, M. Soleilhavoup, P. I. Djurovich, G. Bertrand and M. E. Thompson, *Chem. Commun.*, 2017, **53**, 9008–9011.
32 S. Shi, L. R. Collins, M. F. Mahon, P. I. Djurovich, M. E. Thompson and M. K. Whittlesey, *Dalton Trans.*, 2017, **46**, 745–752.
33 A. M. T. Muthig, J. Wieland, S. Koop, C. Lenczyk, F. Kerner, B. Hupp and A. Steffen, *Inorg. Chem.*, 2022, **61**, 17427–17437.
34 V. A. Krylova, P. I. Djurovich, M. T. Whited and M. E. Thompson, *Chem. Commun.*, 2010, **46**, 6696.
35 R. Visbal and M. C. Gimeno, *Chem. Soc. Rev.*, 2014, **43**, 3551–3574.
36 E. M. Espinoza, J. A. Clark, J. Soliman, J. B. Derr, M. Morales and V. I. Vullev, *J. Electrochem. Soc.*, 2019, **166**, H3175–H3187.
37 V. Q. Dang and T. S. Teets, *Organometallics*, 2024, **43**, 1698–1705.
38 D. Kim and T. S. Teets, *J. Am. Chem. Soc.*, 2024, **146**, 16848–16855.
39 D. Kim, M. C. Rosko, F. N. Castellano, T. G. Gray and T. S. Teets, *J. Am. Chem. Soc.*, 2024, **146**, 19193–19204.
40 T. Neveselý, M. Wienhold, J. J. Molloy and R. Gilmour, *Chem. Rev.*, 2022, **122**, 2650–2694.

41 K. Grudzień, Z. Szeptuch, H. Kubiszewski, W. Chaładaj and K. Rybicka-Jasińska, *J. Org. Chem.*, 2024, **89**, 8546–8550.
42 K. Suzuki, A. Kobayashi, S. Kaneko, K. Takehira, T. Yoshihara, H. Ishida, Y. Shiina, S. Oishi and S. Tobita, *Phys. Chem. Chem. Phys.*, 2009, **11**, 9850.
43 P. G. Seybold and M. Gouterman, *J. Mol. Spectrosc.*, 1969, **31**, 1–13.
44 P. J. Bailey, R. A. Coxall, C. M. Dick, S. Fabre, L. C. Henderson, C. Herber, S. T. Liddle, D. Loroño-González, A. Parkin and S. Parsons, *Chem. – Eur. J.*, 2003, **9**, 4820–4828.
45 D. Hong, Y. Tsukakoshi, H. Kotani, T. Ishizuka and T. Kojima, *J. Am. Chem. Soc.*, 2017, **139**, 6538–6541.
46 G. M. Sheldrick, *Acta Crystallogr., Sect. A: Found. Crystallogr.*, 2008, **64**, 112–122.
47 M. J. Frisch, G. W. Trucks, H. B. Schlegel, G. E. Scuseria, M. A. Robb, J. R. Cheeseman, G. Scalmani, V. Barone, G. A. Petersson, H. Nakatsuji, X. Li, M. Caricato, A. V. Marenich, J. Bloino, B. G. Janesko, R. Gomperts, B. Mennucci, H. P. Hratchian, J. V. Ortiz, A. F. Izmaylov, J. L. Sonnenberg, D. Williams-Young, F. Ding, F. Lipparini, F. Egidi, J. Goings, B. Peng, A. Petrone, T. Henderson, D. Ranasinghe, V. G. Zakrzewski, J. Gao, N. Rega, G. Zheng, W. Liang, M. Hada, M. Ehara, K. Toyota, R. Fukuda, J. Hasegawa, M. Ishida, T. Nakajima, Y. Honda, O. Kitao, H. Nakai, T. Vreven, K. Throssell, J. A. Montgomery Jr., J. E. Peralta, F. Ogliaro, M. J. Bearpark, J. J. Heyd, E. N. Brothers, K. N. Kudin, V. N. Staroverov, T. A. Keith, R. Kobayashi, J. Normand, K. Raghavachari, A. P. Rendell, J. C. Burant, S. S. Iyengar, J. Tomasi, M. Cossi, J. M. Millam, M. Klene, C. Adamo, R. Cammi, J. W. Ochterski, R. L. Martin, K. Morokuma, O. Farkas, J. B. Foresman and D. J. Fox, *Gaussian 16 Rev. C.01*, 2016.
48 C. Adamo and V. Barone, *J. Chem. Phys.*, 1999, **110**, 6158–6170.
49 S. Grimme, S. Ehrlich and L. Goerigk, *J. Comput. Chem.*, 2011, **32**, 1456–1465.
50 S. Grimme, J. Antony, S. Ehrlich and H. Krieg, *J. Chem. Phys.*, 2010, **132**, 154104.
51 P. Schwerdtfeger, M. Dolg, W. H. E. Schwarz, G. A. Bowmaker and P. D. W. Boyd, *J. Chem. Phys.*, 1989, **91**, 1762–1774.
52 A. Schäfer, C. Huber and R. Ahlrichs, *J. Chem. Phys.*, 1994, **100**, 5829–5835.
53 Z. Liu, T. Lu and Q. Chen, *Carbon*, 2020, **165**, 461–467.
54 T. Lu and F. Chen, *J. Comput. Chem.*, 2012, **33**, 580–592.
55 *Blender, version 4.5*, Blender Foundation, Amsterdam, 2024. https://www.blender.org (accessed 10/31/2025).
56 (*a*) CCDC 2418726: Experimental Crystal Structure Determination, 2026, DOI: 10.5517/ccdc.csd.cc2m5wf4; (*b*) CCDC 2418727: Experimental Crystal Structure Determination, 2026, DOI: 10.5517/ccdc.csd.cc2m5wg5.